Acquisition of Spatially-Resolved Displacement Propagators Using Compressed Sensing APGSTE-RARE MRI

Daan W. de Kort[a], Andi Reci[a], Nicholas P. Ramskill[a], Matthias Appel[b], Hilko de Jong[b], Michael D. Mantle[a], Andrew J. Sederman[a], Lynn F. Gladden[a,*]

a) Magnetic Resonance Research Centre, Department of Chemical Engineering and Biotechnology, University of Cambridge, Philippa Fawcett Drive, Cambridge CB3 0AS, United Kingdom

b) Shell Technology Center, 3333 Highway 6 S, Houston TX 77082, USA

[*] Corresponding author
Name: Lynn F. Gladden
Email: lfg1@cam.ac.uk
Tel: (+44) 1223 766338

Keywords: under-sampling, compressed sensing, propagator, MRI, flow, porous media

Revised Manuscript: 14 July 2018

Abstract

A method is presented for accelerating the acquisition of spatially-resolved displacement propagators via under-sampling of an Alternating Pulsed Gradient Stimulated Echo - Rapid Acquisition with Relaxation Enhancement (APGSTE-RARE) data acquisition with compressed sensing image reconstruction. The method was demonstrated with respect to the acquisition of 2D spatially-resolved displacement propagators of water flowing through a packed bed of hollow cylinders. The **q**,**k**-space was under-sampled according to variable-density pseudo-random sampling patterns. The quality of compressed sensing reconstructions of spatially-resolved propagators at a range of sampling fractions was assessed using the peak signal-to-noise ratio (PSNR) as a quality metric. Propagators of good quality (PSNR 33.2 dB) were reconstructed from only 6.25% of all data points in **q**,**k**-space, resulting in a reduction in the data acquisition time from 4 h to 14 min. The spatially-resolved propagators were reconstructed using both the total variation and nuclear norm sparsifying transforms; use of total variation resulted in a slightly higher quality of the reconstructed image in most cases. To illustrate the power of this method to characterise heterogeneous flow in porous media, the method is applied to the characterisation of flow in a vuggy carbonate rock.

1 Introduction

Displacement propagators provide a comprehensive characterisation of fluid motion in porous media, by capturing both the coherent (flow) and incoherent (diffusion and dispersion) contributions. In contrast, magnetic resonance (MR) velocity measurements resolve only the average displacement and are insensitive to the effects of diffusive or dispersive motion [1]. However, the significantly faster data acquisition times characterising a velocity measurement have resulted in the widespread use of spatially-resolved velocity measurements [2], whilst propagators are usually acquired without spatial resolution. Such spatially-unresolved propagator measurements have been used widely in chemical engineering [3-6] and petrophysical [7-10] applications, mainly to study flow dispersion. However, spatially-resolved propagators have been used to characterise transport through heterogeneous porous media under steady-state or slowly-changing conditions when long data acquisition times are acceptable, such as is the case for water transport in plants [11,12]. Therefore, there remains a strong motivation to implement spatially-resolved measurements of propagators in systems that are spatially heterogeneous at length scales comparable to or smaller than the spatial resolution of the velocity map, or for slow-flowing systems in which significant spatial variations in flow dispersion occur. Under such conditions, velocity maps alone may not provide sufficient characterisation of the transport properties of the porous medium. The purpose of the present work is to implement a method which is able to characterise transport heterogeneity in porous media with a particular focus on rock core plugs. The ability to acquire 2D spatially-resolved propagators within a much shorter time frame of order tens of minutes, by using under-sampling and compressed sensing, significantly enhances the ability to study structure-transport relationships in these porous media.

Displacement propagators are probability distributions of molecular displacements $\bar{P}(\mathbf{r}, \Delta)$, where $\bar{P}$ is the probability that a spin moves over a distance $\mathbf{r}$ in an observation time Δ. Spatially-unresolved displacement propagators are routinely acquired using pulsed field gradient (PFG) NMR. The signal intensity A is measured as a function of $\mathbf{q}=\frac{\gamma\delta\mathbf{g}}{2\pi}$, where $\mathbf{g}$ is a vector describing the intensity and direction of the applied gradient pulses, δ the time for which the pulses are applied, and γ the gyromagnetic ratio. $A(\mathbf{q})$ is related to the propagator, for a given Δ, via Fourier transformation (FT):

$$A(\mathbf{q}) = \int \bar{P}(\mathbf{r}, \Delta) \exp[2\pi i \mathbf{q} \cdot \mathbf{r}] d\mathbf{r}, \quad (1)$$

or, inversely,

$$\bar{P}(\mathbf{r}, \Delta) = \int A(\mathbf{q}) \exp[-2\pi i \mathbf{q} \cdot \mathbf{r}] d\mathbf{q}. \quad (2)$$

Acquisition of spatially-resolved displacement propagators can be achieved by combination of a displacement-encoding PFG experiment to acquire **q**-space, and an imaging experiment to acquire **k**-space. Fourier transformation of the combined **q**,**k**-space yields the spatially-resolved propagator.

To accelerate the acquisitions of multi-dimensional data such as spatially-resolved propagators, we have previously demonstrated the use of interpolation of under-sampled **q**-space data to reconstruct a 1D spatially-resolved displacement propagator [13], and the use of **k**-space under-sampling and compressed sensing (CS) to acquire velocity maps in porous media [14] and 3D images of porous media using Rapid Acquisition with Relaxation Enhancement (RARE) MRI [15,16]. Further, Paulsen et al. have demonstrated the use of compressed sensing to accelerate the acquisition of a multi-dimensional diffusive propagator in an anisotropic porous medium [17]. This paper is concerned with combining these different ideas into a method for accelerating the acquisition of 2D spatially-resolved displacement propagators through under-sampling and compressed sensing. The approach presented can be easily extended to acquisition of 3D spatially-resolved propagators.

In Section 2, the basic principles of compressed sensing are outlined. The novel experimental implementation for acquiring under-sampled **q**,**k**-data is described in Section 3. Further details of the experimental acquisitions and samples are described in Section 4.

2 Basic principles of compressed sensing

Because **k**- and **q**-space are equivalent from the mathematical perspective, the principles that apply for under-sampling and compressed sensing of MR images can be directly applied to spatially-resolved propagators. In general, when **q**,**k**-space is under-sampled, an infinite number of equivalent solutions for the spatially resolved-propagator exist that are in agreement with the data. A simple approach to estimate a solution would be by inverse

Fourier transformation of the under-sampled data. Let $\boldsymbol{u}$ denote a spatially-resolved propagator, $\mathcal{F}$ a Fourier transform operator, and S some sampling pattern; the under-sampled (noisy) data $\boldsymbol{y}$ and the (noisy) spatially resolved propagator $\boldsymbol{u}$ are then related through:

$$\boldsymbol{y} = S\mathcal{F}\boldsymbol{u}. \tag{3}$$

Estimating $\boldsymbol{u}$ by inverse Fourier transformation of $\boldsymbol{y}$ will be referred to as the zero-filling (ZF) solution $\boldsymbol{u}_{\mathrm{ZF}}$; i.e., all non-sampled points in $\boldsymbol{y}$ are taken as zero:

$$\boldsymbol{u}_{\mathrm{ZF}} = \mathcal{F}^{-1}S^{\mathrm{T}}\boldsymbol{y}. \tag{4}$$

Because under-sampling of **q**,**k**-space leads to violation of the Nyquist sampling rate, the zero-filling solution $\boldsymbol{u}_{\mathrm{ZF}}$ suffers from artefacts and is sub-optimal. To find a better solution, prior knowledge about the spatially-resolved propagators needs to be incorporated into the reconstruction process. In compressed sensing, the transform sparsity that is implicit in many MR images [18-20], and in propagators [17], is exploited to find a better reconstruction, which we denote $\boldsymbol{u}_{\mathrm{CS}}$. Transform sparsity means that $\boldsymbol{u}$ happens to be sparse in some mathematical transform domain. Using this knowledge, a solution for $\boldsymbol{u}_{\mathrm{CS}}$ is determined subject to the optimisation:

$$\boldsymbol{u}_{\mathrm{CS}} \in \arg\min_{\boldsymbol{u}} \left\{ \frac{1}{2} \|S\mathcal{F}\boldsymbol{u} - \boldsymbol{y}\|_2^2 + \alpha J(\boldsymbol{u}) \right\}, \tag{5}$$

where $\frac{1}{2}\|S\mathcal{F}\boldsymbol{u} - \boldsymbol{y}\|_2^2$ is a fidelity term that ensures consistency with the acquired data, and $\alpha J(\boldsymbol{u})$ is a Tikhonov-regularisation term. $J(\boldsymbol{u})$ is a regularisation functional by which prior knowledge about the transform sparsity of $\boldsymbol{u}$ is incorporated into the optimisation problem. $J(\boldsymbol{u})$ is used to measure the sparsity of $\boldsymbol{u}$ in a certain mathematical transform domain, and the choice of $J(\boldsymbol{u})$ is based on the compressibility of $\boldsymbol{u}$ in that transform domain. The fidelity and regularisation terms are balanced by the regularisation parameter α, which is always a positive number. In this paper, CS reconstructions with a single regularisation term are considered, and the effectiveness of two different regularisation functionals, the total variation (TV) and the nuclear norm (NN), for the reconstruction of spatially-resolved propagators is explored. Total variation regularisation aids in the reconstruction of sharp edges and has already been shown to work well for MR images of heterogeneous porous

media [14-16] and the present work explores whether it also performs well for the reconstruction of spatially-resolved propagators of flow through porous media. Nuclear norm regularisation is a relatively novel approach [21-23] that helps to reconstruct a domain wherein only a limited number of shapes or features exist. Since such a scenario is quite possible for the spatially-resolved propagators expected for describing flow in a porous medium it is of interest to compare the performance of NN with the more widely used TV approach. The TV and NN regularisation functionals are now introduced briefly.

Total variation (TV) regularisation can be used if $\boldsymbol{u}$ can be sparsified by spatial finite-differencing (i.e., by calculating the intensity difference between adjacent pixels). For TV regularisation, $J(\boldsymbol{u})$ is defined as:

$$J(\boldsymbol{u}) = TV(\boldsymbol{u}) = \|\nabla \boldsymbol{u}\|_{\mathbf{2,1}} , \tag{6}$$

where $\|\nabla \boldsymbol{u}\|_{\mathbf{2,1}}$ is the ℓ_1-norm of the ℓ_2-norm of the finite-difference approximation of the local gradient $\nabla \boldsymbol{u}$, with zero Neumann boundary conditions. The ℓ_2-norm of the local gradient, $\|\nabla \boldsymbol{u}\|_{\mathbf{2}}$, may be calculated isotropically (direction-invariant), as in the work of Benning et al. [14], or for specific directions in $\boldsymbol{u}$. Given that for spatially-resolved propagators, the spatial and displacement domains may not need the same degree of TV regularisation, the relative merits of calculating $\|\nabla \boldsymbol{u}\|_{\mathbf{2}}$ in only the spatial domain or in only the displacement domain will also be considered (Section 5.1.3).

Nuclear norm (NN) regularisation [21-23] exploits the potential correlation between the shapes of the individual, spatially-resolved propagators. If these individual propagators are stacked into a matrix $\boldsymbol{U}$ of size $\prod_n^{\mathbf{1-3}} N_{\mathbf{k}_n} \times N_{\mathbf{q}}$ for an *n*-D spatially resolved propagator, where *N* denotes the number of elements in **k** or **q**, the matrix $\boldsymbol{U}$ would have a low rank if the variation between shapes of the individual propagators (i.e., the rows in matrix $\boldsymbol{U}$) is small, since this would result in lower linear independency between the rows of $\boldsymbol{U}$. In the case of NN regularisation, $J(\boldsymbol{u})$ is defined as:

$$J(\boldsymbol{u}) = NN(\boldsymbol{u}) = \|\boldsymbol{U}\|_{\bigstar}, \tag{7}$$

where $\|\boldsymbol{U}\|_\star$ is the nuclear norm or Schatten 1-norm: the sum of singular values resulting from the singular value decomposition of $\boldsymbol{U}$. It is the number of non-zero singular values in $\boldsymbol{U}$ that equals the rank of $\boldsymbol{U}$, but as elsewhere in the implementation of compressed sensing, the minimisation of the nuclear norm (a 1-norm) is used as a convex surrogate for the minimisation of the number of singular values (a 0-norm), and hence for the minimisation of the rank of $\boldsymbol{U}$.

3 Experimental design

In this section, the details of the experimental acquisition of under-sampled spatially-resolved propagators are described. First, the choice of pulse sequence used to acquire the under-sampled **q**,**k**-data is discussed. Second, the under-sampling strategy used in combination with this pulse sequence is described.

3.1 APGSTE-RARE experiment

Rapid imaging methods are based on three broad approaches: (i) the use of small flip angles such as in FLASH [24]; (ii) the recall of the signal from a single excitation of the full magnetization by use of gradient echoes such as in EPI [25]; or (iii) the use of spin echoes such as in RARE [26]. As described by Ramskill et al. [15], RARE imaging is particularly well-suited for under-sampling **k**-space data in the context of spin-density imaging in porous materials and it is therefore the pulse sequence chosen for this study. The two main reasons for using RARE are, first, the magnetization is returned to the same position in **k**-space after acquisition of each echo, allowing a high degree of flexibility in the design of the sampling scheme. Second, in FLASH and EPI, the magnetization is dominated by T_2^* relaxation, whereas in RARE it is dominated by T_2, which is much longer than T_2^* for most porous materials. Furthermore, FLASH is more T_1-limited than RARE and hence in a given time frame the signal-to-noise ratio (SNR) is higher for RARE.

It is important to note that when preceded by a displacement-encoding (i.e., **q**-encoding) pulse sequence, an implementation of RARE using a standard Carr-Purcell-Meiboom-Gill [27,28] phase cycle on the inversion pulse train leads to loss of quadrature due to accumulation of r.f. pulse errors and consequent loss of the phase dispersion that contains the displacement information. Different approaches have been described to overcome this problem, mainly based on separate acquisition of the real and imaginary components of the

signal [29-33], separate acquisition of odd and even-parity echoes [34], or through XY [12,35] or MLEV [36,37] phase cycling. Here, XY phase cycling was used because it keeps the echoes centred such that the Hahn condition is met [38], and hence the echoes T_2^*-compensated, and because it has previously been shown to work robustly in heterogeneous porous media [12]. In this work, a 13-interval alternating pulsed-gradient stimulated echo (APGSTE) experiment [39] was selected for the displacement-encoding PFG experiment preceding the RARE imaging experiment, because it compensates for the phase errors introduced by the internal magnetic field gradients that are present in porous media, and because T_2s of fluids in porous media are often short relative to T_1, thereby justifying the use of a stimulated echo-based PFG experiment.

A schematic of the combined APGSTE-RARE pulse sequence used to acquire 2D spatially resolved propagators is shown in Fig. 1. Each successive pair of odd and even echoes is identically phase-encoded, resulting in two complete **q**,**k**-datasets that are recombined during post-processing. Within each pair of odd and even echoes, Hermitian symmetry exists with respect to the phase development resulting from the displacement-encoding APGSTE experiment [30]. As a consequence, **q**,**k**-space from either the odd or even echoes needs to be flipped around $\mathbf{q} = 0\ \mathrm{m}^{-1}$ before the two datasets are recombined. To allow for addition of the 'flipped' and 'non-flipped' datasets, the **q**-points are sampled symmetrically around $\mathbf{q} = 0\ \mathrm{m}^{-1}$.

3.2 Under-sampling scheme

It is well-established that random under-sampling of **k**-space ensures that artefacts arising from sub-Nyquist sampling add incoherently and appear noise-like [18-20]. The degree of incoherence of applying an sampling pattern in the Fourier domain can be measured by calculating the sidelobe-to-peak ratio (SPR), which is a density-compensated point-spread function [18]; a lower SPR corresponds to greater incoherence. At the cost of some incoherence, pseudo-random, variable-density sampling patterns that sample more densely towards the centre of **k**-space, where the Fourier-coefficients with the highest intensities are located, are typically used for MRI acquisitions. In previous work [15] a pseudo-random pattern generated on the basis of a polynomial probability density function (pdf) has been implemented [18]:

$$\mathrm{pdf}=(1-r)^n, \tag{8}$$

where $r \in 0 < r < 1$ is a measure of distance from the centre of **k**-space, under the limiting constraint that a finite region around the centre of **k**-space is always sampled fully. This ensures that **k**-space is more densely sampled towards the centre than towards the outer edges. The choice of exponent *n* influences the quality of the reconstruction, and is typically chosen such that the width of the pdf qualitatively resembles the Fourier amplitude distribution in **k**-space. For RARE spin-density imaging, only the phase-encoded dimensions $\mathbf{k}_{phase}$ can be sampled according to a variable-density sampling pattern; $\mathbf{k}_{read}$ is sampled at uniform density in lines along $\mathbf{k}_{read}$ for those points sampled in $\mathbf{k}_{phase}$ [15].

For the APGSTE-RARE experiment for acquiring spatially-resolved propagators, additional under-sampling is introduced by varying the number of **k**-space points sampled for each **q**-space point. The number of **k**-space points sampled per **q**-space point is determined randomly on the basis of a pdf similar in shape to the one used for **k**-space. The potentially different distribution of the intensities of the Fourier coefficients in the **q** and **k**-dimensions was adjusted for by varying exponent *n* of the pdf in Eq. 8 cyclically between the $\mathbf{k}_{phase}$ and **q** dimensions as:

$$n_{\mathbf{q},\mathbf{k}_{phase}} = \frac{n_{\mathbf{k}_{phase}}+n_{\mathbf{q}}}{2} + \frac{n_{\mathbf{k}_{phase}}-n_{\mathbf{q}}}{2}\left[2\left(\frac{|\mathbf{k}_{phase}|}{|\mathbf{k}_{phase}+\mathbf{q}|}\right)^2 - 1\right], \quad (9)$$

where $\mathbf{k}_{phase}$ and **q** are vectors pointing towards a specific point in $\mathbf{q},\mathbf{k}_{phase}$-space, and $n_{\mathbf{k}_{phase}}$ and $n_{\mathbf{q}}$ are the exponents along the $\mathbf{k}_{phase}$- and **q**-directions, respectively.

As is evident from the under-sampling scheme outlined in Fig. 2, the sampling pattern using this pdf is subject to two additional constraints imposed by the APGSTE-RARE experiment. The first constraint is that for each point in **q**-space, the number of points in the $\mathbf{k}_{phase}$-dimension(s) should be a multiple of the number of odd/even echo pairs, i.e., half the number of echoes N_{ech}. After the displacement-encoding APGSTE block, a number of lines in **k**-space is read out that equals the number of odd/even echo pairs in the RARE inversion pulse train. Each successive odd/even echo pair is differently phase-encoded, according to the **k**-space sampling pattern for the point in **q**-space that was encoded. The second constraint is that the **q**,**k**-sampling pattern as a whole should be symmetric around $\mathbf{q} = 0\ \mathrm{m}^{-1}$. This allows

reflection of under-sampled **q**,**k**-space from either the odd or even echoes in $\mathbf{q} = 0$ m^{-1}, which ensures that the two data sets can be summed together for post-processing, as described in Section 3.1. The **q**,**k**-sampling patterns subject to these constraints are generated using a modified version of the Monte Carlo approach as described by Lustig et al. [18], and optimised for maximal incoherence on the basis of the SPR. Figure 3 shows the SPR as a function of the degree of sampling and N_{ech} for a series of such **q**,**k**-sampling patterns, subject to these constraints. It is seen that the SPR increases with a decreasing degree of sampling, and with increasing N_{ech}. Three examples of these sampling patterns are shown; it is clearly seen that as N_{ech} increases, the randomness of the sampling pattern decreases, resulting in a higher SPR.

Finally, given the non-uniform sampling density of the **q**,**k**-sampling patterns, the order in which the points are acquired needs to be considered to ensure uniform relaxation weighting throughout **q**,**k**-space. The order in which the points in the **q** and $\mathbf{k}_{phase}$ dimensions are acquired, can be chosen freely; however, only the order in which points in $\mathbf{k}_{phase}$ are acquired will affect relaxation weighting; the order in which points in **q** are encoded does not influence the relaxation weighting. For this reason, to ensure uniform relaxation weighting, the same approach is used for setting the order in which points in $\mathbf{k}_{phase}$ are acquired as was used for non-displacement-encoded under-sampled RARE MRI [15]. In short, the order in which a set of points in $\mathbf{k}_{phase}$ is acquired within each echo train is determined by their distance from the centre of **k**-space. Additionally, for the APGSTE-RARE experiment, phase encoding within each pair of odd and even echoes is identical to allow for recombination of the odd- and even-echo data sets during post-processing. In Fig. 4, an example of a set of phase-encoding trajectories for $N_{\mathrm{ech}} = 32$ is shown. Here, the $\mathbf{k}_{phase}$-points in closest proximity to the centre of **k**-space are acquired in the echoes towards the middle of the RARE loop.

4 Materials and methods

4.1 Experimental Setup

Packed bed of hollow cylinders. A cylindrical random-packed bed was prepared consisting of polyoxomethylene (POM) hollow cylinders (Bülte Plastics). This material has a relatively small difference in magnetic susceptibility relative to water, which minimises the adverse effects of internal magnetic field gradients on the NMR experiments [40]. The bed was packed with a 1:1 mix of cylinders of two different lengths, 4.0 and 6.0 mm, the outer and inner diameter of both being 4.0 and 2.6 mm, respectively. The internal diameter of the bed

was 37 mm and its length was 69 mm. Uniform flow at the entrance and exit was promoted by using porous polyethylene distributor plates (SPC technologies) at either end of the bed. After loading the cylinders into the cylindrical column, the packed bed was imbibed with deionised water through vacuum saturation. The packed bed was connected into a closed flow loop, and a constant flow rate of water of 7 mL min^{-1} was imposed using a Quizix QX-1500 HC dual-cylinder syringe pump.

Vuggy carbonate rock. A cylindrical plug from a vuggy, heterogeneous carbonate outcrop rock of 38.0 mm diameter and 59.7 mm length and an overall porosity of 19.1% was imbibed with deionised water through vacuum saturation. The core was then placed in a cylindrical Ergotech PEEK rock core flow cell. A confining pressure was applied using 3M Fluorinert FC-43, which is NMR silent in typical ^{1}H chemical shift ranges. The flow cell was connected into a closed flow loop, and a constant flow rate of water of 10 mL min^{-1} was imposed using a Quizix QX-1500 HC dual-cylinder syringe pump.

4.2 Magnetic resonance experiments

All NMR measurements were made using a Bruker BioSpin AV spectrometer in combination with a horizontal-bore superconducting magnet with a static field strength B_0 of 2 T (85 MHz ^{1}H resonance frequency) and a birdcage r.f. coil of 60 mm diameter. An Agilent SGRAD MkIII 205/120/HD tri-axial gradient system with a maximum gradient amplitude g_{max} of 0.107 T m^{-1} in the three orthogonal x, y and z-directions was used. The z-direction was defined as the direction of superficial flow through the sample.

4.2.1 Packed bed of hollow cylinders

As a ground truth to benchmark the performance of the under-sampled experiment, a fully sampled 2D spatially-resolved propagator was acquired for the packed bed of hollow cylinders. Gaussian-shaped r.f. pulses of duration 256 μs were used. An axial Gaussian slice of 2.5 mm (FWHM) was selected through the middle of the packed bed. The field-of-view (FOV) in both the $\mathbf{k}_{read}$ and $\mathbf{k}_{phase}$ dimensions was 41 mm, and 128 points were acquired in either direction; thereby giving an in-plane spatial resolution of 320 μm × 320 μm. Thus, local propagators were acquired for each image voxel of in-plane resolution 320 μm × 320 μm, for a slice thickness of 2.5 mm. The number of echoes in the RARE loop N_{ech} was 32 with an echo time, τ_e, of 2.2 ms. For the APGSTE block, the length of a pair of flow-encoding gradients δ was set to 10 ms, and a total of 256 **q**-points were sampled by applying

flow-encoding gradients between -9.63×10^{-2} and 9.63×10^{-2} T m^{-1} (90% of $g_{\max}$) in 256 equidistant steps; i.e., symmetrically around the centre of **q**-space. Displacements were measured along the superficial flow direction, i.e. *z*-direction. The displacement-observation time Δ was 750 ms. Four signal averages were used with a time between excitations of 1.75 s, giving a total acquisition time of 4 h.

After the acquisition, **q**,**k**-space of either the odd and even echoes was flipped in the **q**-dimension. In both data sets, a zeroth-order phase correction was applied according to the phase of the point of maximum intensity, which was also centred in data space. The data from the odd and even echoes were then summed together. To counteract truncation artefacts in the images, a sine window was applied in the $\mathbf{k}_{read}$ and $\mathbf{k}_{phase}$ dimensions, before three-dimensional Fourier transformation in $\mathbf{k}_{phase}$, $\mathbf{k}_{read}$ and **q**. Assuming that an even number of points, $N_{\mathbf{k}}$, is sampled in either **k**-dimension, and that the centre of **k**-space is sampled at the point with index $m = (N_{\mathbf{k}}/2)$, the sine window w is defined as:

$$w(m) = \sin\left(\frac{m\pi}{N_{\mathbf{k}}}\right). \quad (10)$$

Finally, the resulting spatially-resolved propagator was phase corrected in first order.

An under-sampled spatially-resolved propagator was also acquired for the same *x*-*y* image slice. The experiment was set up using the same basic settings as for the fully-sampled experiment. A **q**,**k**-sampling pattern was then generated using the method described in Section 3.2 based on the pdf defined in Eq. 8 and 9, with $n_{\mathbf{k}_{phase}} = 7$ and $n_{\mathbf{q}} = 4$. The resulting sampling scheme sampled 6.25% of the full **q**,**k**-space data points. The resulting acquisition time was 14 min (using 4 averages and a recycle delay 1.75 s). The displacement-observation times was again 750 ms, and the in-plane spatial resolution remained at 320 μm × 320 μm with a slice thickness of 2.5 mm.

The under-sampled data were processed in the same manner as the fully-sampled data, but instead of Fourier transformation, compressed sensing reconstruction was performed using a primal-dual hybrid gradient method as described in detail elsewhere [14,41,42].

4.2.2 Vuggy carbonate rock plug

2D spatially-resolved propagators were also acquired for the vuggy carbonate rock plugs. The data acquisition parameters were as follows. The number of echoes in the RARE loop N_{ech} was reduced to 8 with an echo time, τ_e, of 2.2 ms. For the APGSTE block, the displacement-observation time Δ was reduced to 300 ms. These changes were made because of the shorter T_1 and T_2 of the water inside the carbonate rock. The FOV in both the $\mathbf{k}_{read}$ and $\mathbf{k}_{phase}$ dimensions was set to 45 mm, and 128 points were acquired in either direction (i.e., the in-plane spatial resolution was 352 μm × 352 μm); the slice thickness was 2.5 mm. A new sampling pattern was generated, based on the same pdf using the same approach as described in Section 4.2.1 but taking into account the lower N_{ech}. By acquiring 8 averages at a recycle delay 2 s, the acquisition time for the fully-sampled experiment was 37 h, and for the under-sampled experiment 2 h 18 min.

5. Results and discussion

The following section is structured as follows. In Section 5.1 the effect of the three aspects of the pulse sequence implementation that have been used to yield spatially-resolved propagators on the quantitative nature of the displacement measurement are reported and discussed. Sections 5.2 and 5.3 report acquired spatially-resolved propagators in the model system and a vuggy carbonate rock, respectively.

5.1 Evaluation of the quality of reconstructed local propagators

To achieve the measurement of under-sampled spatially-resolved propagators, three modifications to a standard spatially-unresolved propagator acquisition are required: the XY-phase cycling within the RARE sequence; the introduction of spatial resolution into the propagator measurement; and the details of the CS reconstructions. The effect of each of these on the accuracy of the measured propagator is discussed.

5.1.1 Phase cycling within the RARE sequence

Application of phase cycles such as XY [12,35] and MLEV [36,37] during an inversion pulse train prevents problems resulting from the accumulation of imperfections in the pulses; higher-order (i.e., longer) cycles provide better compensation. Ahola et al. [30] have presented an in-depth analysis of the phase evolution of the magnetisation when applying such phase cycles. Their conclusion was that although the phase cycles provide significant

compensation for pulse errors, the original phase of the signal is only fully conserved in the even-parity echoes– and the odd-parity echoes should therefore be discarded. Indeed, the phase of the odd and even echoes is not precisely the same, but their phase is constant throughout the echo train. Further, as has been demonstrated by Van As and co-workers [43], two individually phase-encoded **q**,**k**-data sets can be acquired in the odd and even echoes, which are then phase-corrected individually. Because of the Hermitian symmetry between the odd and even echoes, either the odd- or the even-echo data can then be reflected in $\mathbf{q} = 0\ \mathrm{m}^{-1}$ after which the odd and even echoes can be summed to improve the signal-to-noise ratio. Figure 5 shows the total spatially-unresolved propagator for flow in the packed bed of cylinders, obtained by summation of the individual spatially-resolved propagators, for both the odd- and even-echo (fully-sampled) data. It is seen that the total propagators are indistinguishable. The same holds for the individual, per-pixel propagators. Henceforth, all propagators shown will be based on the recombination of the odd and even echo data.

5.1.2 Introduction of spatial resolution to the propagator measurement

To further demonstrate that the application of RARE has no significant effect on the accuracy of the propagators, the total propagator obtained from summing the individual per-pixel propagators (fully-sampled) is compared to (1) the total propagator obtained from using only the central **k**-space point from the same **q**,**k**-data, and (2) the total propagator measured by a standalone slice-selective APGSTE experiment. As can be seen in Fig. 6, the propagators resulting from these three methods are indistinguishable.

To assess the accuracy of the per-pixel propagators themselves, a comparison is made between the mean velocity calculated from the per-pixel propagators, and a flow velocity map calculated from the per-pixel phase difference, $\Delta\varphi$, between two images acquired at two different values of **q**, where $\varphi = 2\pi\mathbf{q}\cdot\mathbf{v}\Delta$, with **v** being the average local fluid velocity. These two images were obtained by applying a Fourier transform to the **q**,**k**-data in the two **k**-dimensions, and selecting two images at either side of $\mathbf{q} = 0\ \mathrm{m}^{-1}$. The two velocity maps and the associated velocity distributions are shown in Fig. 7b and 7c and Fig. 7d and 7e, respectively. The intensity image of the slice from which the data are taken is shown in Fig. 7a. The superficial flow direction is perpendicular to this image slice. There is good agreement between the map of mean velocity calculated from the spatial-resolved propagator measurements (Fig. 7b) and the directly acquired velocity map (Fig. 7c). The velocity distributions calculated from the propagator measurements (Fig. 7d) and directly from the

velocity map (Fig. 7e) are not expected to be identical because the latter method is based on the calculation of a phase average, and because of a difference in SNR between the two approaches, as can be seen from the larger noise level in the velocity map of Fig. 7c compared to that of Fig. 7b. Nevertheless, the mean velocity of the distribution calculated from the propagator measurements (206±2 μm s^{-1}) is in agreement with the distribution calculated from the velocity map (208±2 μm s^{-1}) to within experimental error. The standard deviation of the distribution calculated from the propagator measurements (237±1 μm s^{-1}) is smaller, but of the same order as that determined for the distribution derived from the velocity measurements (273±1 μm s^{-1}). This difference is expected to be largely due to the larger root mean square error in the velocity map-derived velocities relative to the propagator-derived velocities, discussed earlier. The error in velocity map-derived velocities is proportional to the SNR of the underlying image [44] and equals 61 μm s^{-1} on average for the map in Fig. 7c, which is of the same order as the difference in standard deviation between the propagator-derived and velocity map-derived velocity distributions of Fig. 7d and e, respectively. In summary, the good agreement of the velocity data calculated from the propagators with the directly measured velocity data confirmed that the introduction of spatial resolution into the propagator measurement has retained the accuracy of the propagator measurement.

5.1.3 Sensitivity to details of the CS reconstructions

The fully-sampled spatially-resolved propagators are now compared to the compressed sensing reconstructions of under-sampled spatially-resolved propagators. As a quality metric for the quality of the reconstructions, the peak signal-to-noise ratio (PSNR) is used, which is defined as:

$$\mathrm{PSNR}(\boldsymbol{u}_{\mathrm{CS}}, \boldsymbol{u}_{\mathrm{FS}}) = 20\log_{10}\left[\frac{\max(\boldsymbol{u}_{\mathrm{FS}})}{\|\boldsymbol{u}_{\mathrm{CS}}, \boldsymbol{u}_{\mathrm{FS}}\|_2^2 / N_{\mathrm{pix}}}\right], \tag{11}$$

where $\boldsymbol{u}_{\mathrm{CS}}$ and $\boldsymbol{u}_{\mathrm{FS}}$ are the spatially-resolved propagators obtained through compressed sensing reconstructions of under-sampled propagators and from Fourier transformation of the fully- sampled data, respectively, and N_{pix} is the number of pixels (or voxels for a volume image) in $\boldsymbol{u}$. PSNR is normally expressed in units of dB; a higher value is indicative of a better reconstruction quality. A perfect reconstruction has PSNR = ∞ dB.

The effects of the degree of sampling and of N_{ech} on the compressed sensing reconstruction quality were assessed. In Fig. 8, reconstruction quality as measured by PSNR is shown for the various sampling patterns of which the SPRs are shown in Fig. 3. The different patterns were applied to the fully-sampled dataset, which was truncated to 128 points in the **q**-dimension to save computation time. The reconstruction qualities obtained through isotropic TV regularisation and NN regularisation are also compared in Fig. 8. A range of values for the regularisation parameter α were considered to find the optimal reconstruction quality in terms of PSNR for a given sampling pattern. An initial broad search of α-values was used to identify the range in which the maximum in PSNR was located – the search for the optimal α-value was then narrowed down to this range to find the best value for α. A fully-sampled ground truth for optimisation of α would normally not be available in an actual application of this method. It was therefore verified that under those circumstances, Morozov's discrepancy principle [45] provides an adequate estimate of α as compared the optimal-PSNR solution, as was previously demonstrated by Benning et al. to also be the case for CS MRI velocity experiments [14].

With regard to TV regularisation, isotropic TV regularisation ($TV_{\mathbf{q},\mathbf{k}}$) was also compared with TV regularisation in only the **k**-dimensions ($TV_{\mathbf{k}}$) or in only the **q**-dimension ($TV_{\mathbf{q}}$). It was shown that $TV_{\mathbf{q},\mathbf{k}}$ outperforms $TV_{\mathbf{k}}$ or $TV_{\mathbf{q}}$. For example, for the sampling pattern with N_{ech} = 2 and 50% sampling, $TV_{\mathbf{q},\mathbf{k}}$ resulted in a PSNR of 35.5 dB, $TV_{\mathbf{k}}$ in a PSNR of 35.1 dB and $TV_{\mathbf{q}}$ in a PSNR of 33.2 dB. $TV_{\mathbf{q}}$ did significantly improve the reconstruction quality relative to the zero-filled (ZF) solution (PSNR = 32.1 dB), from which it can be concluded that TV is an adequate regulariser for the displacement domain. Since this analysis showed that TV improves reconstruction of features present in both the displacement and spatial domains, only isotropic TV regularisation ($TV_{\mathbf{q},\mathbf{k}}$) is considered in further comparisons.

The data in Fig. 8 show that TV and NN regularisation both perform well, but TV regularisation generally outperforms NN regularisation. It is seen that TV regularisation yields significantly better results for higher N_{ech} (i.e., for patterns with a higher SPR). At higher sampling levels, for $N_{ech} < 20$, the performance of NN and TV converge, with the reconstructions of 50% sampled datasets being of the same quality. However, for the application to the spatially-resolved propagators shown in this work it was noted that NN regularisation led to much more rapid convergence of the optimisation problem ($\sim 10^2$ iterations for NN, 10^3 for TV), and that the individual iterations were less computationally

expensive (NN ~2× faster than TV). Therefore, in those cases wherein the quality of reconstructions generated using TV and NN regularisation are similar, NN may become the regulariser of choice when dealing with the much larger datasets characteristic of 3D spatially-resolved propagators. There exists some variability in PSNR depending on the specific sampling pattern used, which is a result of the outcome of the optimisation procedure of the sampling pattern based on SPR, in combination with the exact distribution of Fourier coefficients in **q**,**k**-space.

On the basis of this analysis, the datasets acquired using the under-sampled APGSTE-RARE experiment were sampled at 6.25% and reconstructed using only isotropic TV regularisation.

5.2 Spatially-resolved propagators within the model system

The nature and quality of data obtained are illustrated in Fig. 9. A spatially-resolved propagator is acquired for each 320 μm × 320 μm pixel within the image. Figure 9a shows the total intensity image obtained by projecting the data within each pixel along the **q**-dimension. Three pixels are then identified, positioned at the tip of each arrowhead. The spatially-resolved propagators associated with pixels 1, 2 and 3 are shown in Fig. 9b, c and d, respectively. In each of these figures, three propagators are shown which have been calculated from a direct Fourier transform of the fully-sampled data; the zero-filled transform of the 6.25% sampled data; and the compressed sensing reconstruction of the 6.25% sampled data, reconstructed using TV regularisation.

First, the general form of the spatially-resolved propagators associated with the three pixels are discussed. These data demonstrate the insights that can be gained from spatial resolution of the propagator measurement. Further, by studying this model system, the ability of the measurement to capture local flow dispersion in this system are assessed. The degree of per-voxel flow dispersion is quantified by calculating the displacement standard deviation $\sigma_{\mathbf{r}}$ [46]:

$$\sigma_{\mathbf{r}} = (\langle \mathbf{r}(\Delta)^2 \rangle - \langle \mathbf{r}(\Delta) \rangle^2)^{1/2}, \qquad (12)$$

where **r** is the displacement along the flow-encoded direction over observation time Δ, and $\langle \mathbf{r}(\Delta) \rangle$ (the mean displacement) and $\langle \mathbf{r}(\Delta)^2 \rangle$ are given by:

$$\langle \mathbf{r}(\Delta) \rangle = \frac{\int \bar{P}(\mathbf{r},\Delta)\mathbf{r}\mathrm{d}\mathbf{r}}{\int \bar{P}(\mathbf{r},\Delta)\mathrm{d}\mathbf{r}}, \langle \mathbf{r}(\Delta)^2 \rangle = \frac{\int \bar{P}(\mathbf{r},\Delta)\mathbf{r}^2\mathrm{d}\mathbf{r}}{\int \bar{P}(\mathbf{r},\Delta)\mathrm{d}\mathbf{r}}, \quad (13)$$

where $\bar{P}(\mathbf{r},\Delta)$ is the propagator. Considering pixel 1 (Fig. 9a) it is seen that the pixel lies within a hollow cylinder which lies perpendicular to the direction of superficial flow. The propagator obtained from this pixel (Fig. 9b) takes the form of a Gaussian distribution centred around a mean displacement of only 21 μm with a standard deviation of 57 μm, i.e. the flow is near-stagnant within the orthogonally aligned hollow cylinder. The mean-square displacement of water molecules due to self-diffusivity, $\sqrt{2D\Delta}$, where D is the self-diffusion coefficient (2.0×10^{-9} m^2 s^{-1} for water at 293 K) and Δ=750 ms, equals 55 μm – a close match to the displacement in standard deviation of the propagator. In contrast to pixel 1, pixel 2 (Fig. 9c) lies within a cylinder aligned along the superficial flow direction. In this case the propagator again takes a Gaussian form but with a mean displacement of 262 μm with a standard deviation of 58 μm; in this location there is coherent flow, and the propagator is broadened only by the self-diffusivity of the water molecules. Finally, pixel 3 (Fig. 9d) is located outside any cylinder and the propagator assumes a broader, skewed shape with a mean displacement of 726 μm and a standard deviation of 145 μm; at this position, significant additional dispersion in excess of self-diffusivity is observed, due to the water molecules having passed through a region of high shear. The distribution is also significantly skewed. Therefore, for this pixel, a single velocity would not be an adequate representation of the local flow characteristics, which illustrates how spatially-resolved propagators can contribute to our understanding of flow in complex geometries.

With reference to Fig. 9b–d, the performance of the three propagators reconstructed for pixels 1, 2 and 3 are now compared. It is clearly seen that the fully-sampled Fourier transformed and TV-regularised CS-reconstructed propagators are in excellent agreement. In contrast, the under-sampled, zero-filled and Fourier transformed propagators are significantly different and suffer from artefacts that are absent in the Fourier transformation of the fully-sampled data. Closer inspection of the propagators shows that the TV-regularised compressed sensing reconstruction of the under-sampled data significantly improves the quality of the propagators beyond that of the zero-filled Fourier transformed data. This is also reflected by the PSNR of the zero-filled Fourier transform and of the TV reconstruction relative to the Fourier transform of the fully-sampled data: the zero-filled FT has a PSNR of 30.9 dB and

CS with isotropic TV regularisation has a PSNR of 33.2 dB. It is noted that the PSNRs for the CS reconstruction of the under-sampled experiment are inherently limited by the fact that it is a comparison to a separately acquired fully-sampled experiment, between which subtle changes in flow field may have occurred. Further, it is seen that the noise level of the fully-sampled Fourier transformed propagators is higher than that of the TV-regularised CS-reconstructed propagators. This is because the CS reconstructions are inherently denoising. Although it would be possible to subject the fully-sampled data to the same treatment as the under-sampled data, which would lead to a similar degree of denoising, only the result for the Fourier transform is shown here because it is the conventional way of treating fully-sampled data.

In Fig. 10a, a comparison is made between the spatially-unresolved propagator obtained using the same three approaches discussed in Fig. 9. Again, compressed sensing can be seen to improve the quality of the spatially-unresolved propagator significantly with respect to the zero-filled FT of the 6.25% sampled data. In Fig. 10b, displacement images are shown for two specific displacements (0 μm and 256 μm). These displacement images are spatially-resolved maps of the relative probability of a molecule of the fluid displacing over that distance. As expected, it is seen that the compressed sensing reconstructions are of superior quality relative to the zero-filled FT. The bright-yellow rectangular areas seen in the 0 μm displacement images (an example is indicated by arrow 1) correspond to areas within cylinders that are aligned perpendicular to the superficial flow direction; the water in these regions is near-stagnant and hence these areas do not show up in the 256 μm displacement image. The many ring-shaped features that can be seen in both the 0 μm and 256 μm displacement images are characteristic of an approximately parabolic (Hagen-Poiseuille) flow profile inside cylinders oriented along the direction of superficial flow; such parabolic flow profiles are also seen in the velocity maps of Fig. 7b. The ring-shaped features in the 0 μm displacement images (see arrow 2) are of larger diameter than the same features in the 256 μm displacement images, because the lowest displacements are found near the interface between the fluid and the cylinders, and the higher displacements are found towards the centre of the cylinders.

5.3 Spatially-resolved propagators within a vuggy carbonate rock

Figure 11 shows a comparison of the total propagator obtained by summation of the individual per-pixel propagators from a fully-sampled, spatially-resolved experiment with a

total propagator obtained from a spatially-unresolved acquisition. The agreement is excellent. This is particularly interesting because it confirms that any effects of relaxation during the RARE pulse train can be kept to a minimum. Broad, trimodal distributions of both T_1 (mean 0.65 s) and T_2 (mean 0.65 s) were observed for water in the pores of the vuggy carbonate rock, reflecting its heterogeneous pore size distribution. Further, the result confirms that internal gradients that can be expected to be present within the carbonate rock do not significantly influence the spatially-resolved propagator with respect to the spatially-unresolved result.

The 2D spatially-resolved propagator for flow through the vuggy carbonate rock plug is presented in Fig. 12. A propagator is acquired for each in-plane pixel of 352 μm × 352 μm. In Fig. 12a, the spatial heterogeneity of the rock is clearly seen. Fig. 12b, c and d show the spatially-resolved propagators from pixels 1, 2 and 3 respectively.

As was the case for the packed bed, the local propagators assume a variety of different shapes. Pixel 1 lies adjacent to a cluster of pixels of fast flow (yellow shades) and yet is associated with near-stagnant flow (mean displacement 6 μm, standard deviation 39 μm). As was the case in the packed bed, the standard deviation is comparable to the mean-square displacement due to self-diffusivity at an observation time Δ=300 ms, which is 35 μm. Pixels 2 and 3 are separated by a distance of only 1.4 mm and lie within regions containing flowing liquid. However, as seen from Fig. 11c and d, their propagators are very different. Pixel 2 is associated with a propagator of mean displacement of 310 μm with a standard deviation of 283 μm. The corresponding data for pixel 3 are characterised by a mean displacement of 115 μm with a standard deviation of 141 μm.

A comparison of the three propagators calculated at each of these spatial locations leads to similar observations as for the model packed bed. Compressed sensing is seen to improve the quality of the under-sampled propagator relative to the zero-filling solution ($PSNR_{ZF}$ = 36.1 dB; $PSNR_{TV}$ = 36.7 dB).

6. Conclusions

Multi-dimensional magnetic resonance experiments such as the acquisition of spatially-resolved propagators are often considered too time-consuming to perform because of the large number of data points that need to be acquired. The present work exploits the fact that

as the dimensionality of the data increases, the reduction of experimental acquisition time due to under-sampling increases, because of the multiplicative effect of under-sampling multiple dimensions.

A method to experimentally under-sample spatially-resolved propagators using an APGSTE-RARE pulse sequence with a pseudo-random, variable-density sampling pattern has been implemented. Demonstration of the method on a model system of water flow in a packed bed of hollow cylinders confirmed that the acquired propagators were robust to the phase cycle with the imaging sequence, the introduction of spatial resolution into the measurement and the details of the CS reconstruction. By sampling **q**,**k**-space by 6.25%, a 16-fold reduction of acquisition time was achieved relative to the fully-sampled experiment. Compressed sensing reconstructions using TV regularisation and NN regularisation were compared, and it was found that TV outperforms NN regularisation in most cases.

The method was then applied to water flow through a vuggy carbonate rock, and it was confirmed that the effect of relaxation within the RARE pulse train was minimal. This is an important result since these are the types of porous media which will be a particular focus of future study. Ongoing work is addressing the extension of this method to 3D spatial resolution of propagators where it is expected that even greater reductions in acquisition time can be gained relative to the fully-sampled data acquisition as a result of the higher dimensionality of the data acquisition.

Acknowledgments

The authors would like to thank Royal Dutch Shell plc for funding this work. A.R. acknowledges Gates Trust Cambridge for financial support.

References

[1] A.J. Sederman, L.F. Gladden, Magnetic resonance visualisation of single- and two-phase flow in porous media, Magn. Reson. Imaging 19 (2001) 339–343. doi:10.1016/s0730-725x(01)00246-6.

[2] L.F. Gladden, A.J. Sederman, Recent advances in Flow MRI, J. Magn. Reson. 229 (2013) 2–11. doi:10.1016/j.jmr.2012.11.022.

[3] J. Park, S.J. Gibbs, Mapping flow and dispersion in a packed column by MRI, AIChE J. 45 (1999) 655–660. doi:10.1002/aic.690450322.

[4] M.D. Mantle, A.J. Sederman, L.F. Gladden, Single- and two-phase flow in fixed-bed reactors: MRI flow visualisation and lattice-Boltzmann simulations, Chem. Eng. Sci. 56 (2001) 523–529. doi:10.1016/s0009-2509(00)00256-6.

[5] E.L. Gjersing, S.L. Codd, J.D. Seymour, P.S. Stewart, Magnetic resonance microscopy analysis of advective transport in a biofilm reactor, Biotechnol. Bioeng. 89 (2005) 822–834. doi:10.1002/bit.20400.

[6] B. Manz, L.F. Gladden, P.B. Warren, Flow and dispersion in porous media: Lattice-Boltzmann and NMR studies, AIChE J. 45 (1999) 1845–1854. doi:10.1002/aic.690450902.

[7] R.A. Waggoner, E. Fukushima, Velocity distribution of slow fluid flows in bentheimer sandstone: An NMRI and propagator study, Magn. Reson. Imaging 14 (1996) 1085–1091. doi:10.1016/s0730-725x(96)00110-5.

[8] U.M. Scheven, J.G. Seland, D.G. Cory, NMR-propagator measurements in porous media in the presence of surface relaxation and internal fields, Magn. Reson. Imaging 23 (2005) 363–365. doi:10.1016/j.mri.2004.11.054.

[9] J. Mitchell, A.J. Sederman, E.J. Fordham, M.L. Johns, L.F. Gladden, A rapid measurement of flow propagators in porous rocks, J. Magn. Reson. 191 (2008) 267–272. doi:10.1016/j.jmr.2007.12.014.

[10] R. Hussain, T.R.R. Pintelon, J. Mitchell, M.L. Johns, Using NMR displacement measurements to probe CO_2 entrapment in porous media, AIChE J. 57 (2010) 1700–1709. doi:10.1002/aic.12401.

[11] T.W.J. Scheenen, D. van Dusschoten, P.A. de Jager, H. Van As, Quantification of water transport in plants with NMR imaging, J. Exp. Bot. 51 (2000) 1751–1759. doi:10.1093/jexbot/51.351.1751.

[12] C.W. Windt, F.J. Vergeldt, H. Van As, Correlated displacement–T_2 MRI by means of a Pulsed Field Gradient-Multi Spin Echo method, J. Magn. Reson. 185 (2007) 230–239. doi:10.1016/j.jmr.2006.12.015.

[13] A.A. Colbourne, A.J. Sederman, M.D. Mantle, L.F. Gladden, Accelerating flow propagator measurements for the investigation of reactive transport in porous media, J. Magn. Reson. 272 (2016) 68–72. doi:10.1016/j.jmr.2016.08.018.

[14] M. Benning, L. Gladden, D. Holland, C.-B. Schönlieb, T. Valkonen, Phase reconstruction from velocity-encoded MRI measurements – A survey of sparsity-promoting variational approaches, J. Magn. Reson. 238 (2014) 26–43. doi:10.1016/j.jmr.2013.10.003.

[15] N.P. Ramskill, I. Bush, A.J. Sederman, M.D. Mantle, M. Benning, B.C. Anger, et al., Fast imaging of laboratory core floods using 3D compressed sensing RARE MRI, J. Magn. Reson.. 270 (2016) 187–197. doi:10.1016/j.jmr.2016.07.017.

[16] N.P. Ramskill, A.J. Sederman, M.D. Mantle, M. Appel, H. de Jong, L.F. Gladden, In Situ Chemically-Selective Monitoring of Multiphase Displacement Processes in a

Carbonate Rock Using 3D Magnetic Resonance Imaging, Transport Porous Med. 121 (2018) 15-35. doi:10.1007/s11242-017-0945-6.
[17] J.L. Paulsen, H. Cho, G. Cho, Y.-Q. Song, Acceleration of multi-dimensional propagator measurements with compressed sensing, J. Magn. Reson. 213 (2011) 166–170. doi:10.1016/j.jmr.2011.08.025.
[18] M. Lustig, D. Donoho, J.M. Pauly, Sparse MRI: The application of compressed sensing for rapid MR imaging, Magn. Reson. Med. 58 (2007) 1182–1195. doi:10.1002/mrm.21391.
[19] M. Lustig, D.L. Donoho, J.M. Santos, J.M. Pauly, Compressed Sensing MRI, IEEE Signal Process. Mag. 25 (2008) 72–82. doi:10.1109/MSP.2007.914728.
[20] D.J. Holland, L.F. Gladden, Less is more: How compressed sensing is transforming metrology in chemistry, Angew. Chem. Int. Ed. 53 (2014) 13330–13340. doi:10.1002/anie.201400535.
[21] D. Xiao, B.J. Balcom, k-t Acceleration in pure phase encode MRI to monitor dynamic flooding processes in rock core plugs, J. Magn. Reson. 243 (2014) 114–121. doi:10.1016/j.jmr.2014.04.006.
[22] T. Zhang, J.M. Pauly, I.R. Levesque, Accelerating parameter mapping with a locally low rank constraint, Magn. Reson. Med. 73 (2014) 655–661. doi:10.1002/mrm.25161.
[23] B. Zhao, W. Lu, T.K. Hitchens, F. Lam, C. Ho, Z.-P. Liang, Accelerated MR parameter mapping with low-rank and sparsity constraints, Magn. Reson. Med. 74 (2014) 489–498. doi:10.1002/mrm.25421.
[24] A. Haase, J. Frahm, D. Matthaei, W. Hänicke, K.D. Merboldt, FLASH imaging: Rapid NMR imaging using low flip-angle pulses, J. Magn. Reson. 213 (2011) 533–541. doi:10.1016/j.jmr.2011.09.021.
[25] P. Mansfield, Multi-planar image formation using NMR spin echoes, J. Phys. C: Solid State Phys. 10 (2001) L55–L58. doi:10.1088/0022-3719/10/3/004.
[26] J. Hennig, A. Nauerth, H. Friedburg, RARE imaging: A fast imaging method for clinical MR, Magn. Reson. Med. 3 (1986) 823–833. doi:10.1002/mrm.1910030602.
[27] H.Y. Carr, E.M. Purcell, Effects of Diffusion on Free Precession in Nuclear Magnetic Resonance Experiments, Phys. Rev. 94 (1954) 630–638. doi:10.1103/physrev.94.630.
[28] S. Meiboom, D. Gill, Modified Spin-Echo Method for Measuring Nuclear Relaxation Times, Rev. Sci. Instrum. 29 (1958) 688–691. doi:10.1063/1.1716296.
[29] J. Perlo, F. Casanova, B. Blümich, 3D imaging with a single-sided sensor: an open tomograph, J. Magn. Reson. 166 (2004) 228–235. doi:10.1016/j.jmr.2003.10.018.
[30] S. Ahola, J. Perlo, F. Casanova, S. Stapf, B. Blümich, Multiecho sequence for velocity imaging in inhomogeneous rf fields, J. Magn. Reson. 182 (2006) 143–151. doi:10.1016/j.jmr.2006.06.017.
[31] P. Galvosas, P.T. Callaghan, Fast magnetic resonance imaging and velocimetry for liquids under high flow rates, J. Magn. Reson. 181 (2006) 119–125. doi:10.1016/j.jmr.2006.03.020.
[32] S. Kuczera, P. Galvosas, Advances and artefact suppression in RARE-velocimetry for flow with curved streamlines, J. Magn. Reson. 259 (2015) 135–145. doi:10.1016/j.jmr.2015.07.015.
[33] L. Huang, G. Mikolajczyk, E. Küstermann, M. Wilhelm, S. Odenbach, W. Dreher, Adapted MR velocimetry of slow liquid flow in porous media, J. Magn. Reson. 276 (2017) 103–112. doi:10.1016/j.jmr.2017.01.017.

[34] G. Shiko, A.J. Sederman, L.F. Gladden, MRI technique for the snapshot imaging of quantitative velocity maps using RARE, J. Magn. Reson. 216 (2012) 183–191. doi:10.1016/j.jmr.2012.01.021.
[35] T. Gullion, D.B. Baker, M.S. Conradi, New, compensated Carr-Purcell sequences, J. Magn. Reson. 89 (1990) 479–484. doi:10.1016/0022-2364(90)90331-3.
[36] M.H. Levitt, Composite pulses, Prog. Nucl. Mag. Res. Sp. 18 (1986) 61–122. doi:10.1016/0079-6565(86)80005-x.
[37] T.W.J. Scheenen, D. van Dusschoten, P.A. de Jager, H. Van As, Microscopic Displacement Imaging with Pulsed Field Gradient Turbo Spin–Echo NMR, J. Magn. Reson. 142 (2000) 207–215. doi:10.1006/jmre.1999.1916.
[38] E.L. Hahn, Spin Echoes, Phys. Rev. 80 (1950) 580–594. doi:10.1103/PhysRev.80.580.
[39] R.M. Cotts, M.J.R. Hoch, T. Sun, J.T. Markert, Pulsed field gradient stimulated echo methods for improved NMR diffusion measurements in heterogeneous systems, J. Magn. Reson. 83 (1989) 252–266. doi:10.1016/0022-2364(89)90189-3.
[40] M.C. Wapler, J. Leupold, I. Dragonu, D. von Elverfeld, M. Zaitsev, U. Wallrabe, Magnetic properties of materials for MR engineering, micro-MR and beyond, J. Magn. Reson. 242 (2014) 233–242. doi:10.1016/j.jmr.2014.02.005.
[41] A. Chambolle, T. Pock, A first-order primal-dual algorithm for convex problems with applications to imaging, J. Math. Imaging Vis. 40 (2010) 120–145. doi:10.1007/s10851-010-0251-1.
[42] A. Chambolle, T. Pock, An introduction to continuous optimization for imaging, Acta Numer. 25 (2016) 161–319. doi:10.1017/S096249291600009X.
[43] T.W.J. Scheenen, F.J. Vergeldt, C.W. Windt, P.A. de Jager, H. Van As, Microscopic imaging of slow flow and diffusion: A pulsed field gradient stimulated echo sequence combined with turbo spin echo imaging, J. Magn. Reson. 151 (2001) 94–100. doi:10.1006/jmre.2001.2362.
[44] P.T. Callaghan, Translational Dynamics and Magnetic Resonance, OUP, Oxford, 2011.
[45] V.A. Morozov, Regularization of incorrectly posed problems and the choice of regularization parameter, USSR Comput. Math. & Math. Phys. 6 (1966) 242–251. doi:10.1016/0041-5553(66)90046-2.
[46] B. Manz, P. Alexander, L.F. Gladden, Correlations between dispersion and structure in porous media probed by nuclear magnetic resonance, Phys. Fluids 11 (1999) 259–267. doi:10.1063/1.869876.

Figure captions

Figure 1: Pulse sequence to acquire 2D spatially-resolved propagators, which consists of a 13-interval APGSTE sequence followed by an XY-phase cycled RARE sequence. In the RARE sequence, an XY-16 (*x y x y y x y x –x –y –x –y –y –x –y –x*) phase cycle is used for the 180° inversion pulses. Each successive pair of odd and even echoes is identically phase-encoded in $\mathbf{k}_{phase}$, so that two separate spatially-resolved propagators are acquired that can be added together during post-processing. The directions of displacement (**q**) and spatial (**k**) encoding can be chosen independently. In this work, the slice direction and the direction of flow encoding were both parallel to the superficial flow direction *z*.

Figure 2: Schematic of the under-sampling protocol. For each excitation, only a single **q**-value can be encoded into the signal. This implies that t
he number of **k**-space points acquired per **q**-space point must be a multiple of half the number of echoes (N_{ech}) in the RARE experiment, since each successive pair of odd and even echoes in the RARE-train is identically phase-encoded.

Figure 3: Pseudo-random, variable-density sampling patterns are used to sample the **q**-dimension and the phase-encoded dimension(s) $\mathbf{k}_{phase}$. (a) Sidelobe-to-peak ratio for a range of different pseudo-random **q**,$\mathbf{k}_{phase}$-sampling patterns to be used with the APGSTE-RARE experiment, for different values of N_{ech} and degrees of sampling: (●) 50%, (■) 25%, (▲) 12.5%, (▼) 6.25%. The patterns had sizes of $\mathbf{k}_{phase}$ × **q** = 128×128 points, and were generated on the basis of a pdf as in Eq. 8 with $n_{\mathbf{k}_p}$, $n_{\mathbf{q}}$ = 7; 50,000 random sampling patterns were generated from which the pattern with the lowest SPR was selected. (b-d) Three examples of sampling patterns that illustrate the effect of increasing N_{ech}. The white pixels correspond to the positions at which a line in the readout dimension $\mathbf{k}_{read}$ is sampled. It can be seen that the patterns are symmetrical in **q** = 0 m^{-1} to allow for addition of the odd and even echoes during post-processing.

Figure 4: Four representative sampling trajectories for the phase encoding direction $\mathbf{k}_{phase}$. The order in which a set of points in $\mathbf{k}_{phase}$ is acquired within each echo train, is determined on the basis of their distance from the centre of **k**-space; for the example shown, N_{ech} = 32, and $N_{\mathbf{k}}$, $N_{\mathbf{q}}$ = 128. Each successive pair of odd and even echoes is identically phase-encoded.

Figure 5: Comparison of the even-echo (——) and odd-echo (- - -) total displacement propagators obtained by addition of the individual, per-pixel propagators from the fully-sampled, 2D spatially-resolved propagator for flow in the packed bed. The two propagators are indistinguishable, justifying addition of the two datasets for post-processing.

Figure 6: Comparison of the total displacement propagator associated with a 2D slice obtained by three different methods: Summation of the individual, per-pixel propagators from a fully-sampled, 2D spatially-resolved experiment; i.e., a projection along **k** (——); a spatially-unresolved 13-interval APGSTE experiment (– – –); calculated from the central **k**-space points for every **q**-value from the combined odd- and even-echo spatially resolved data and Fourier transformation along **q** (- - -).

Figure 7: Assessment of the accuracy of the spatially-resolved propagators. The intensity image (a) is shown as a reference. The superficial flow direction is perpendicular to the image slice and velocities were measured along the superficial flow direction. Velocity maps are shown for (b) propagator-derived velocities and (c) velocimetry-derived velocities. (d) and (e) show the velocity distributions calculated from (b) and (c) respectively.

Figure 8: Variation of the PSNR of the compressed sensing reconstructions of spatially resolved propagators as a function of the degree of sampling and N_{ech}, reconstructed using the isotropic TV (closed symbols) and NN (open symbols) as regularisation functionals. The SPRs of the sampling patterns that were used, are shown in Figure 3a. **TV**: (●) 50% sampling, (■) 25%, (▲) 12.5%, (▼) 6.25%. **NN**: (○) 50%, (□) 25%, (△) 12.5%, (▽) 6.25%. The lines serve as guides for the eye.

Figure 9: 2D spatially-resolved propagator for water flow through the packed bed of hollow cylinders. In the fully-sampled intensity image (a), arrows indicate three locations (1–3) for which the local propagators are shown (b-d). Local propagators are shown for an observation time of 750 ms. A comparison is made between local propagators obtained from fully-sampled, Fourier transformed data (——), with data acquired at 6.25% sampling followed by: zero-filling and Fourier-transformation (– – –), and the TV-regularised CS reconstruction (– – –). The under-sampled data were acquired using the APGSTE-RARE experiment.

Figure 10: (a) Comparison of the total (i.e., spatially-unresolved) propagator obtained from summation of 2D spatially-resolved propagators acquired using 3 approaches: fully-sampled followed by Fourier transformation (——); 6.25% sampling, zero-filling followed by Fourier-transformation (– – –); and 6.25% sampling, followed by TV-regularised CS reconstruction (– – –). The under-sampled data were acquired using the under-sampling APGSTE-RARE experiment. (b) Two displacement images showing maps of populations of 0 and 256 μm flow displacements, respectively. These displacements are indicated by the dotted lines on the total propagator shown in (a). The total propagator and the displacement images are shown on the same probability scale.

Figure 11: Comparison of the total displacement propagator associated with a 2D slice through a vuggy carbonate rock obtained by two different methods: Summation of the individual, per-pixel propagators from a fully-sampled, 2D-spatially resolved experiment; i.e., a projection along **k** (——); and a non-spatially-resolved 13-interval APGSTE experiment (– – –).

Figure 12: 2D spatially-resolved propagator for water flow through the vuggy carbonate rock. In the fully-sampled intensity image (a), arrows indicate three locations (1–3) for which the local propagators are shown (b-d). Local propagators are shown for an observation time of 300 ms. A comparison is made between the fully-sampled, Fourier transformed data (——), and the 6.25% sampled data: under-sampled, zero-filled and Fourier-transformed (– – –), and TV-regularised with CS reconstruction (– – –). The under-sampled data were acquired using the under-sampling APGSTE-RARE experiment.

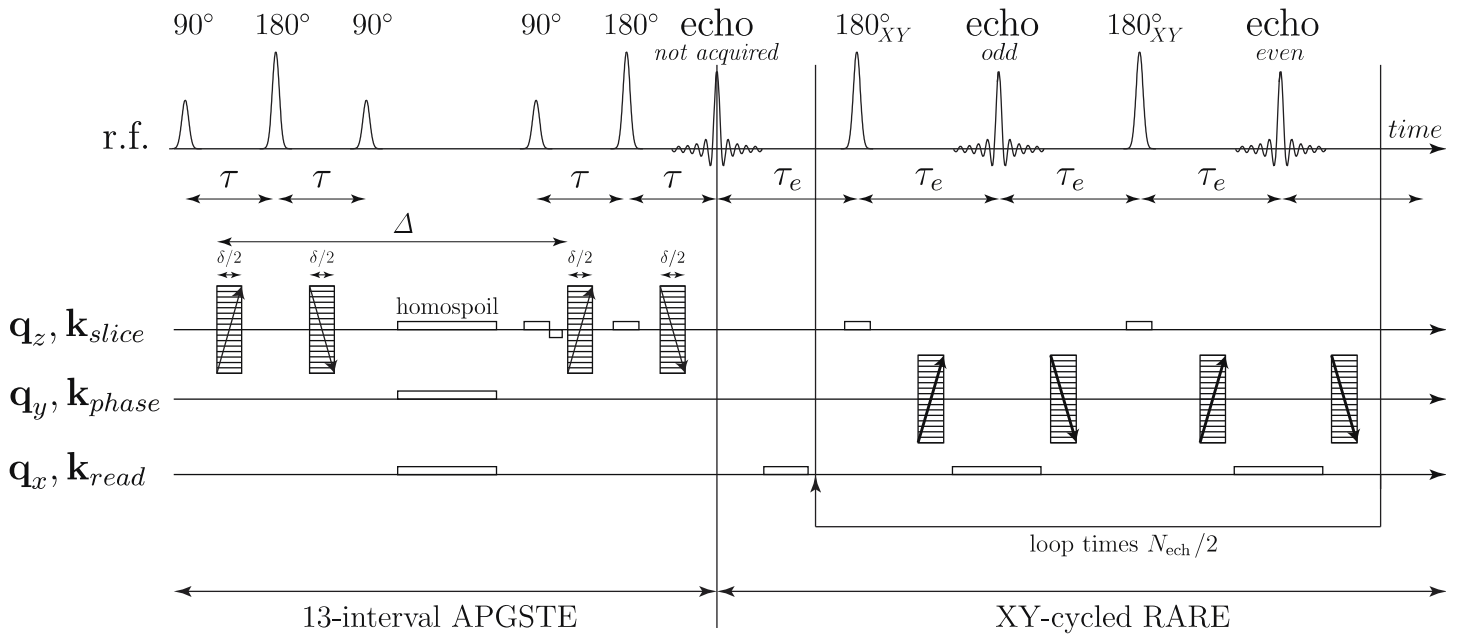

Figure 1 – 2 column (width 19 cm)

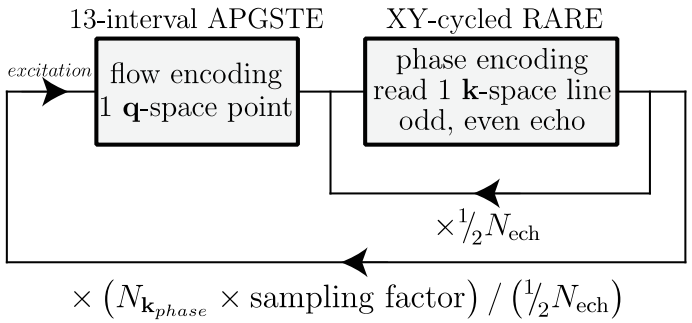

Figure 2 – 1 column / 9 cm

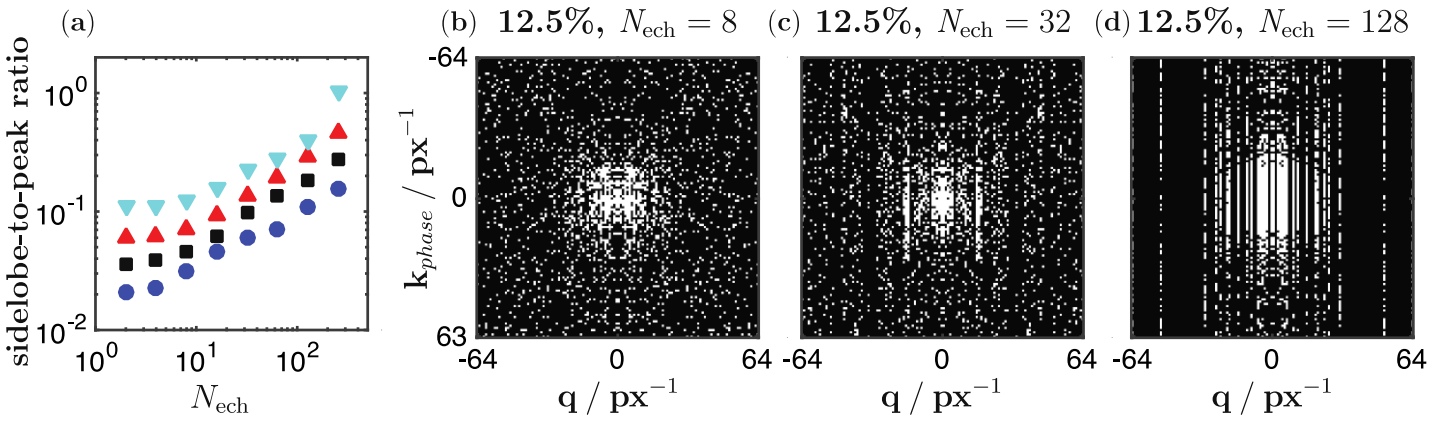

Figure 3 – 2 column / 19 cm

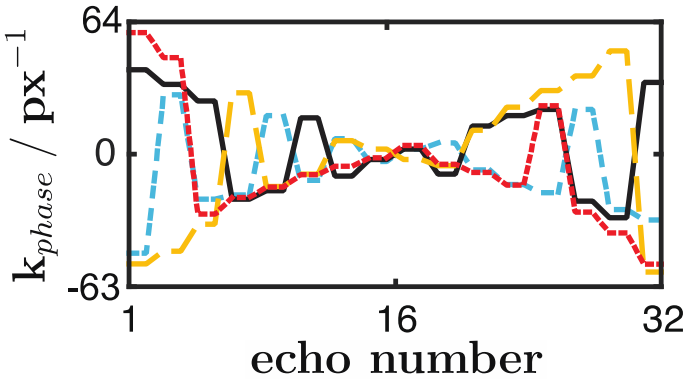

Figure 4 – 1 column / 9 cm

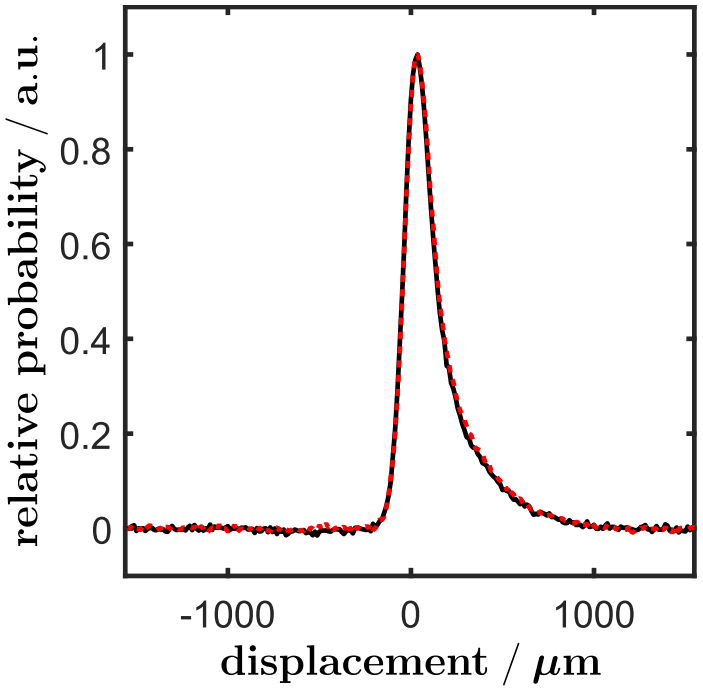

Figure 5 – 1 column / 9 cm

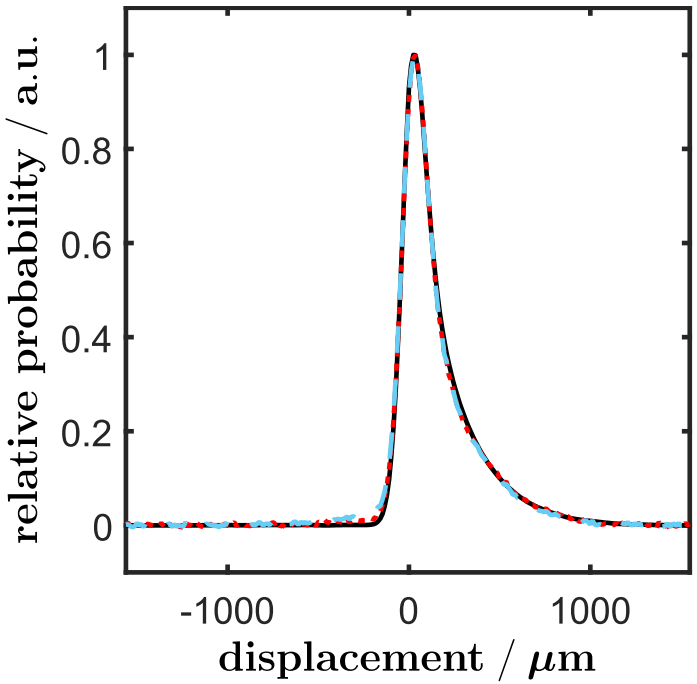

Figure 6 - 1 column / 9 cm

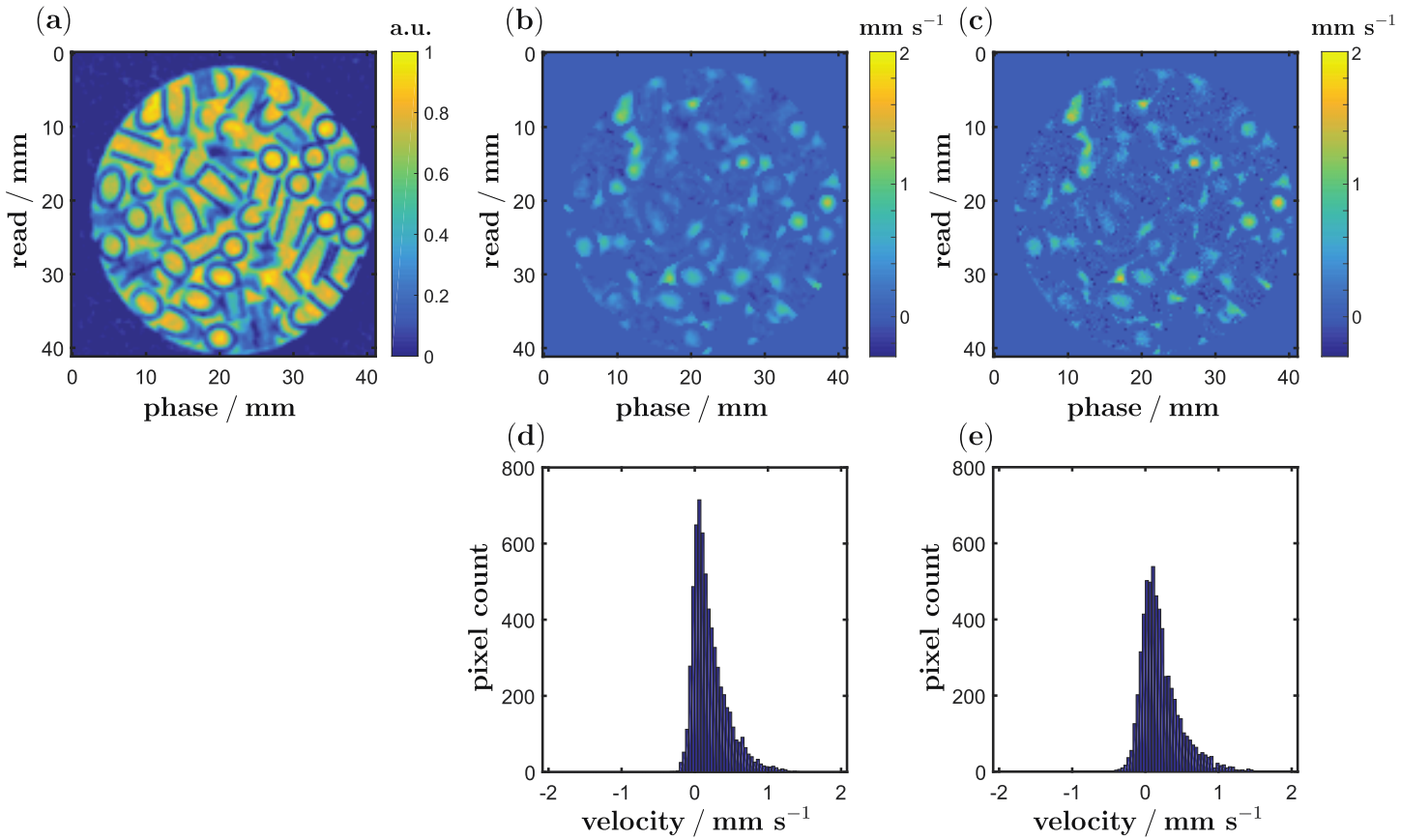

Figure 7 – 2 column / 19 cm

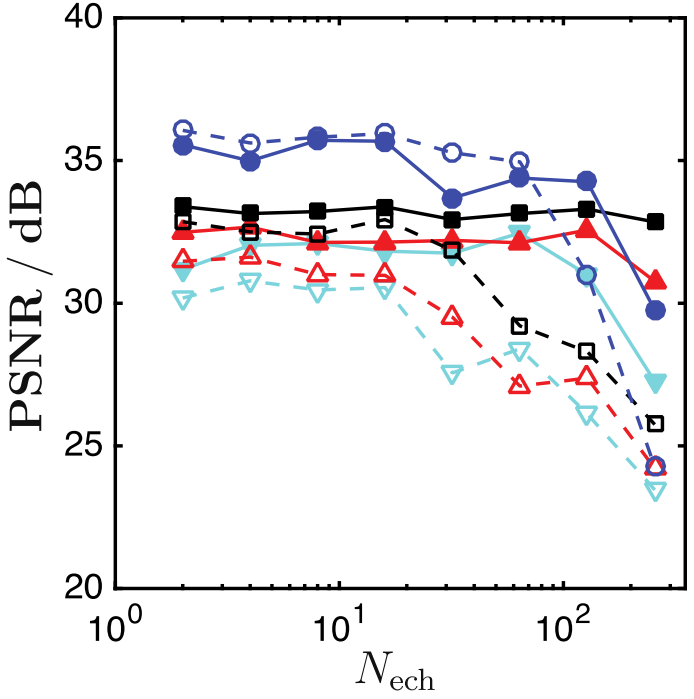

Figure 8 – 1 column / 9 cm

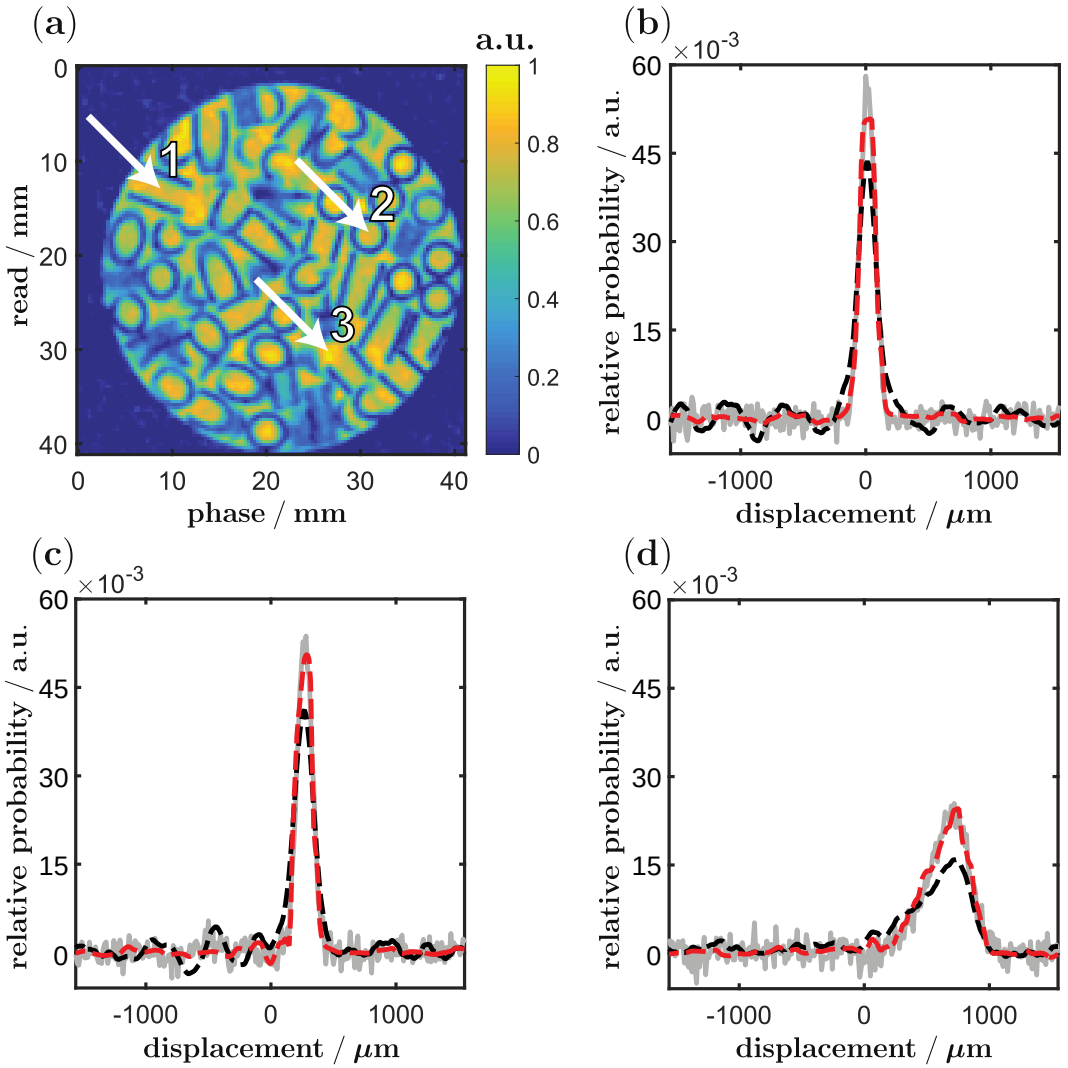

Figure 9 – 1.5 column / 14 cm

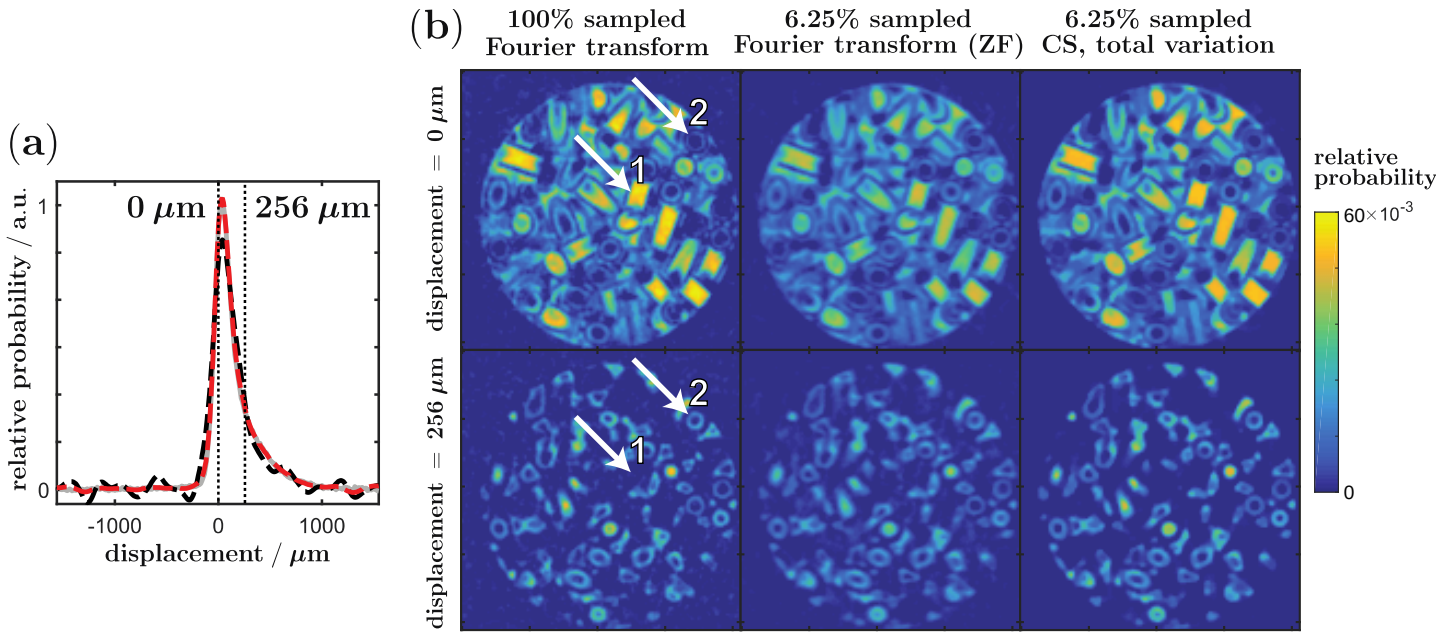

Figure 10 – 2 column / 19 cm

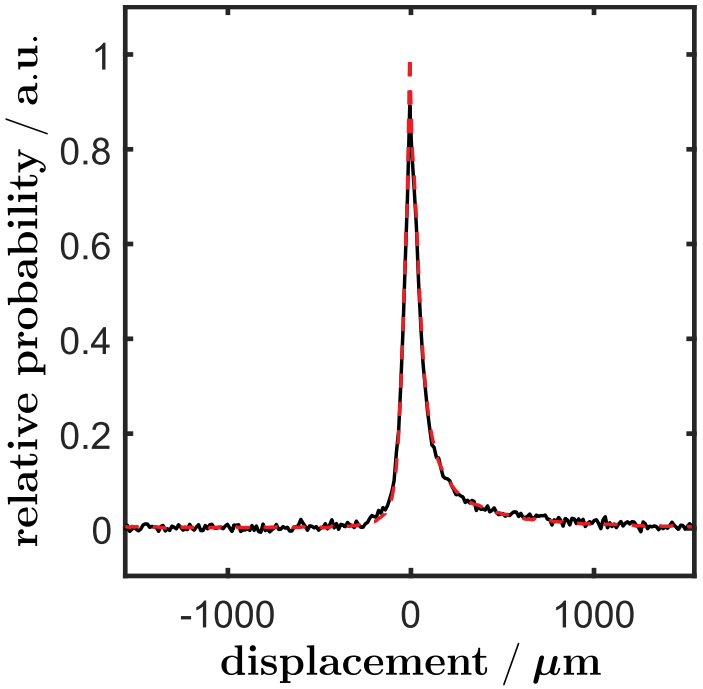

Figure 11 – 1 column / 9 cm

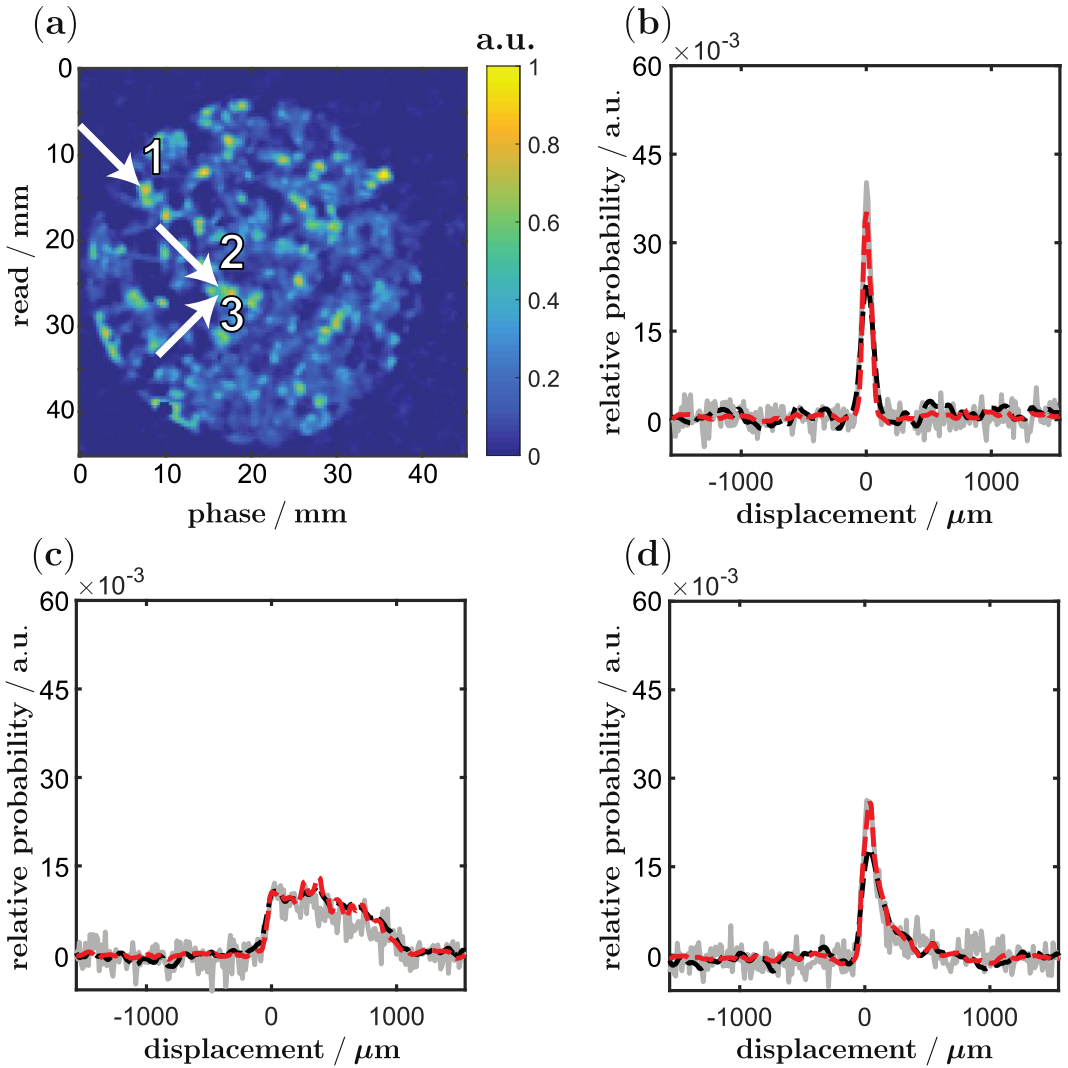

Figure 12 – 1.5 column / 14 cm